Journal of Solar Energy Research (JSER)

Journal homepage: www.jser.ut.ac.ir

Performance Enhancement of Solar Air Heater with Different Roughness Absorber Plates

Musaab K. Rasheed[a], Hussian A. Abdul kareem[b], Fadhil Abdulrazzaq Kareem[a], Mudhar A. Al-Obaidi[c*]

[a]*Institute of Technology-Baghdad, Middle Technical University, Baghdad 10074, Iraq*
[b]*Technical Engineering College -Baghdad, Middle Technical University, Baghdad 10074, Iraq*
[c]*Technical Instructor Training Institute, Middle Technical University, Baghdad 10074, Iraq*

ARTICLE INFO

Article Type:

Research Article

Received:2025.08.19
Accepted in revised form:2025.09.26

Keywords:
Double Pass Air Heater (DPSAH);
Turbulators;
CFD Simulation;
Thermo-Hydraulic Performance;
Heat Transfer Coefficient

A B S T R A C T

This research assesses the heat transfer and performance attributes of the double-pass air heater (DPSAH) integrated with turbulators through a 3D CFD simulation methodology. DPSAH setup comprises of a rectangular channel divided by an absorber plate with double baffles; the lower side of the plate provides five fins in the flow direction, while the upper side of the plate provides eight different geometries. The numerical model has been validated against analytical and experimental findings gathered from the open literature with a satisfactory degree of deviance. Results demonstrate that wave plates improve heat transfer relative to smooth surfaces. This signifies that THPP increases with increasing Reynolds number. Although increased friction and decreased pressure require enhanced pumping power to maintain mass flow, the efficiency advantages at higher Reynolds numbers justify the extra energy expenditure. The turbulator significantly enhances the operational efficiency of the DPSAH in the absorber section. The wave plate exhibits a markedly elevated exit temperature and sufficient performance compared to the other cross-sectional geometries. Numerical estimations suggest that a waved surface can enhance the efficiency of a solar air heater by 14%. The results indicate an elevated airflow rate resulting from a reduced outlet temperature and an enhanced pressure drop.

1. Introduction

Solar energy is considered one of the most promising future sources as a result of its cost-free, clean, and readily accessible characteristics [1,2]. Several solar air heater (SAH) types were used to convert solar energy into thermal energy [3] systematically. Among the current solar thermal technologies, SAHs are extensively utilised for space heating, agricultural product drying, and

*Corresponding Author Email: dr.mudhar.alaubedy@mtu.edu.iq

Cite this article: Rasheed, M. K. , Abdul kareem, H. Ali , Kareem, F. Abdulrazzaq and Al-Obaidi, M. A. (2025). Performance Enhancement of Solar Air Heater with Different Roughness Absorber Plates. Journal of Solar Energy Research, 10(2), 2367-2382. doi: 10.22059/jser.2025.400971.1622

DOI: 10.22059/jser.2025.400971.1622

photovoltaic cooling [4,5]. SAH is a system that uses an absorber to convert solar energy into thermal energy to heat air that circulates via a duct. The air is heated through contact with the absorbing plate, which transfers the captured solar heat to the circulating air that departs via the output duct, supplying warm air for diverse heating applications [6-8]. Nonetheless, a significant drawback of SAH is the diminished convective heat transfer between the absorbing plate and the ambient air. This phenomenon is chiefly attributed to the formation of a Laminar Sub-Layer (LSL) on the heat-exposed surface, hence affecting the overall system efficiency and performance [9-12].

Numerous studies have sought to advance the heat transfer rates in SAH by adjusting the design of the absorber plate. The solar air collector's performance in North Eastern India's climates was experimentally examined by Debnath et al. 2018 [13]. The findings indicated that the double-glazing absorber plate consistently demonstrates superior performance from both exergy and energy perspectives. A rise in air mass flow rate can lead to enhanced energy competence. Implementing corrugated plates can also result in a 14% increase in energy efficiency. The peak improvement in exergy competence for the double-glazing collector is 6.867% at a mass flow rate of 0.0118 kg/s in comparison to the single-glazing collector.

The thermal performance of an impinging jet double-pass solar air heater was experimentally explored by Singh et al. 2020 [14]. The maximum thermal efficiency and thermo-hydraulic efficiency achieved for SAH without porous media are 94% and 84%, respectively, representing an increase of approximately 7.5% and 19% in comparison to SAH with porous media.

The performance of an SAH was experimentally presented by Hassan and AboElfadl, 2021 [15]. The supreme transverse SAH energy efficacy value of approximately 89% was attained under double-pass airflow conditions and a high air mass flow rate of 0.075 kg/s, representing a 24.2% improvement relative to flat plate SAH. Although the air pumping power of transverse SAH exceeds that of flat plate SAH, its impact on net energy gain was minimal.

Iqbal et al. (2023) [16] numerically evaluated a new configuration of SAH that features an integrated setup of impinging air jets and rectangular-sectioned V-ribs on the absorber surface. The results showed a significant increase of 3.36 in Nusselt number and 5.31 in friction factor compared to traditional SAHs under similar boundary conditions. The research concluded that the proposed jet cooling configuration with rectangular-sectioned V-ribs is an effective way to enhance SAH performance.

A trapezoidal rib was studied to advance the thermal action of the SAH by Hamad et al. (2023) [17]. The flow and heat transfer characteristics were numerically analysed utilising an RNG k-turbulent model predicated on the Reynolds number. The findings indicated that optimal thermal performance of the solar collector occurred when the ribs were affixed and removed from the inner wall surface, with an enhancement in the height of the trapezoidal ribs oriented against the airflow for all rib configurations. The thermal performance exhibited its lowest levels in scenarios where the attached or detached trapezoidal ribs' height increased in the airflow direction.

Singh and Kumar (2024) [18] focused on experimental and simulation efforts aimed at optimising the thermal characteristics, specifically the friction factor (f) and Nusselt number (Nu), alongside the roughness configurations defined by e/Dh, e/d1, and d1/d2 for frustum-shaped roughened elements. The results indicated that the optimal value of Nu = 256.77 can be observed at 'e/Dh', 'e/d1', and 'd1/d2' ratios of 0.043, 0.98, and 2.33, respectively, while using Re = 12500. The friction factor reached its minimum value of 0.009 at the following parameters: e/Dh = 0.014, e/d1 = 1.44, d1/d2 = 2.06, and Re = 12158 via maximising the value of Nu to 256.77 and minimising the value of f to 0.009, which achieved the desirability of 0.0905.

Chang et al. (2024) [19] investigated the influence of the number of transverse baffles (N) on flow and heat transfer features in SAHs, indicating that an increase in N can result in a corresponding rise in both the intensity and size of the vortex zones. This change significantly affected the heat transfer dynamics between the air and the absorber plate. Amongst the analyzed values of N (2, 4, 6, and 8), at a flow rate of 0.026 kg s^{-1}, N = 4 demonstrated the highest competence, recorded at 54.32%. In contrast, for mass flow rates of 0.039 kg/s, 0.052 kg/s, 0.065 kg/s, and 0.078 kg/s, the maximum competence was recorded at N = 6, yielding values of 60.03%, 63.78%, 64.39%, and 64.38%, respectively.

Yusaidi et al. (2024) [20] presented an investigation that includes both theoretical and experimental analyses regarding the impact of a DPSAH using staggered-diamond-shaped fins. The maximum thermal efficacy achieved in both experiment and simulation was 59.34% and 62.01%, respectively, at a mass flow rate of 0.0261 kg/s under solar irradiance of 1000 W/m^2. The mass flow

rate rose from 0.01044 kg/s to 0.0261 kg/s, resulting in an enhanced energy efficiency of the collectors.

Salarpour and Azadani (2024) [21] presented an analysis of the fluid flow and heat transfer features of SAHs featuring six distinct roughness geometries: inline cubical elements, rectangular baffles, staggered cubical elements, V-shaped baffles, square ribs, and V-shaped ribs. The results indicated that the rectangular baffles can exhibit the highest Nusselt number and thermo-hydraulic performance parameter, whereas the inline cubical elements demonstrated the lowest performance.

Rawat and Sherwani (2024) [22] presented a 2D transient model for an SAH incorporating phase change material (PCM). The findings indicated that an increase in the thickness-to-length ratio (t/L) can result in an enhancement in peak liquid fraction. Thus, the system's exergy and energy efficacies were enhanced. In a single pass flow system, the optimisation of t/L at 0.042 can result in a peak liquid fraction of 0.928, a decrease in dead length by 92.28%. In a double-pass flow system, the optimised t/L ratio of 0.058 yielded a peak liquid fraction of 0.976.

Dong et al. (2025) [23] investigated a cost-effective and well-organized approach to improve the energy productivity of progressive photovoltaic/thermal (PV/T) collectors. In comparison to a fixed PV/T system lacking a reflector, the multi-hybrid approach demonstrated a relative enhancement of 17.76% in thermal gain and 13.61% in electrical gain for the innovative PV/T configuration featuring graphite and trapezoidal fluid channels. This corresponds to energy outputs of 39.5 MJ and 7.8 kWh, based on an effective area of 2.08 m². The literature review has been condensed and displayed in Table A1 of Appendix A.

Previous investigations on SAHs have predominantly concentrated on the influence of baffle geometry and dimensional alterations; however, a comprehensive assessment of the dual positioning of baffles on both the upper and lower surfaces of the absorber plate in double-pass solar air heaters (DPSAHs) has not been conducted yet. The current research attempts to fill this gap in the open literature by employing advanced three-dimensional numerical simulations to systematically examine the thermo-hydraulic behavior across diverse baffle shapes and strategic placements. The research explicitly evaluates and compares the local convective heat transfer coefficients, thermal efficiency, and overall thermo-hydraulic performance of the analysed models. This research presents a novel investigation of baffle placement within the air channel of DPSAHs, demonstrating that thermo-hydraulic performance can be significantly enhanced not only by modifying baffle geometry but also through their strategic positioning.

2. Numerical method

2.1 Physical model

The numerical simulations for airflow in the DPSAH were precisely carried out using COMSOL Multiphysics 6.1. This process involves accurate modeling of the flow domain geometry, careful mesh generation, and thorough equation solving, all performed seamlessly within the COMSOL environment. This comprehensive approach guarantees both the accuracy and reliability of the current simulation results [24-28].

2.2 Geometry

The DPSAH configuration comprises a rectangular channel divided by an absorber plate. A schematic representation of the DPSAH is depicted in Fig. 1. The channel sizes are 86 cm long, 40 cm wide, and 9.5 cm high. An aluminum absorber with a thickness of 1 mm is used, featuring rectangular-section fins on its bottom surface. Details of the impingement plate are presented in Table 1. Figure 2 illustrates the superior perspectives of a segment of the absorber section featuring various roughness geometries. The roughness characteristics evaluated in this research are also displayed in Fig. 2. Six different roughness geometries, comprising corrugate plate, wave plate, orifice fins in line, orifice fins staggered, V-ribs in line, V-ribs staggered, S-ribs in line, S-ribs staggered, are utilised.

Table 1. Dimensions of the main parts of the DPSAH model

Dimension	Value (cm)
Glass cover	86x40x0.4
Absorber plate	80x40x3.5
Aluminum fins	80x0.5x4
Number fins	5
Air cover	86x40x9.5
Space between the glass cover and the Absorber plate	2
Space between the back cover and plate	4

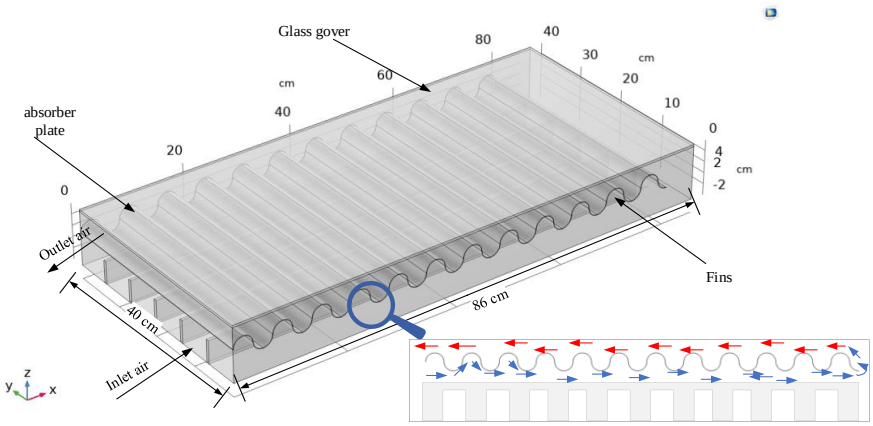

Figure 1. A schematic diagram of the DPSAH

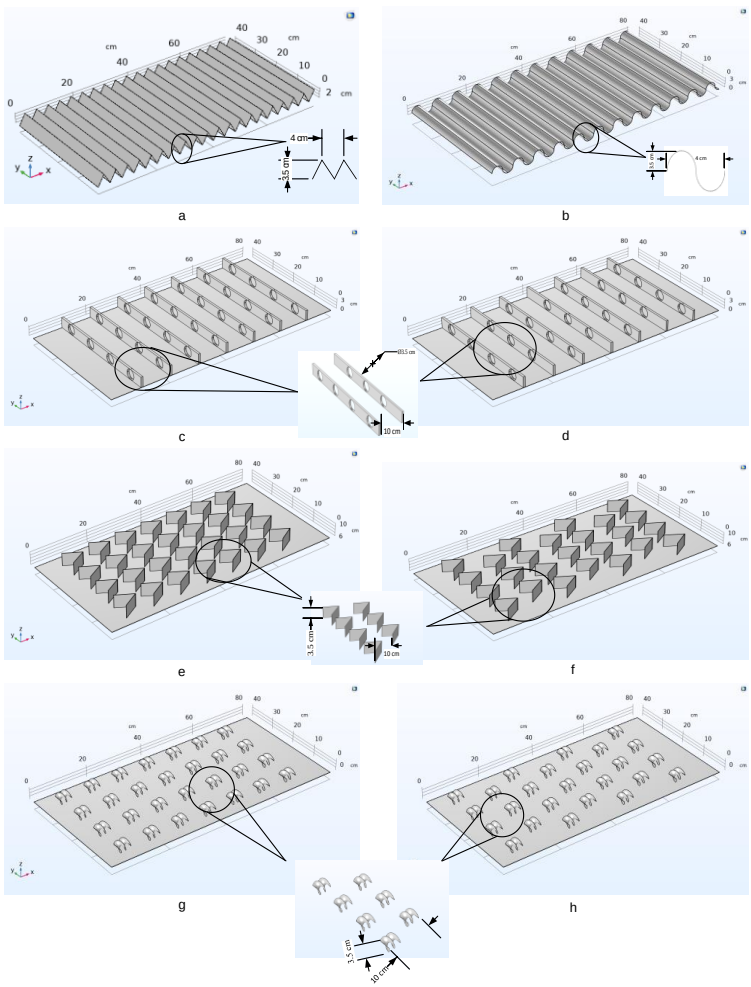

Figure 2. Various roughness geometries used in the current research: (a) corrugate plate, (b) wave plate, (c) orifice fins in line, (d) orifice fins staggered, (e) V-ribs in line, (f) V-ribs staggered, (g) S-ribs in line, (h) S-ribs staggered

2.3 Assumptions

The succeeding presumptions were considered in the formulation and solution of the present DPSAH simulation model:

1.To effectively optimise the numerical analysis of incompressible and turbulent fluid flows through channels, the RANS k-ε model was strategically employed to investigate minimising DPSAH. This approach streamlines computational efficiency and enhances the accuracy of the results.

2.Analysing unsteady-state conditions related to three-dimensional heat transfer within a computational domain is essential to improve the understanding of thermal behaviors. By carefully examining these dynamic processes, more accurate predictions can be made, and optimising the designs would result in more efficient thermal management solutions.

3.The bottom and side surfaces of the DPSAH air channel are meticulously insulated, ensuring they are entirely adiabatic. This strategic design would enhance the thermal efficiency by minimising heat loss, making the system more effective and reliable.

4.Temperature significantly influences the fluid's thermo-physical features, highlighting the critical importance of temperature dependence in understanding fluid behavior.

5.The DPSAH's physical characteristics, such as viscosity, density, heat capacity, and thermal conductivity, are temperature-dependent.

6.The temperature of ambient conditions and solar radiation varies with time, illustrating the dynamic relationship between environmental factors and their effects throughout the day.

2.4 Initial and Boundary Conditions

Based on the computational domain shown in Figure 3, the initial and boundary conditions for fluid and solid walls are as follows:

1- Solid surface (Walls Heat Transfer): The no-slip condition applies to solid walls, where the velocity components were set to zero (u = 0, v = 0, w = 0). Also, there was no thermal jump at the wall surface. The adiabatic condition holds for insulated surfaces (q = 0 or dq = 0).

2- Aluminum Plate: The boundary walls are in non-slip conditions, and the sides of the aluminum layers are assumed to be thermally insulated. The interfaces between the aluminum and the channels are considered coupled interfaces.

3- Fluid flow: The inlet air temperature with air velocity, and at the outlet of the channel was "Pressure Outlet" with a static pressure of p 0. Gravity has not been factored into this simulation.

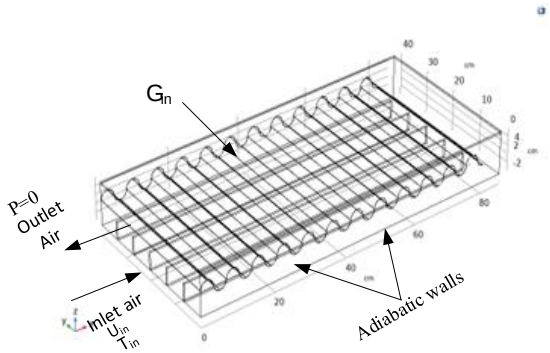

Figure 3. 3-D schematic view and boundary conditions

2.5 Governing equations

The fluid flow and heat transfer features of air in DPSAH were investigated numerically by solving the Reynolds-Averaged Navier-Stokes (RANS) correlations alongside the energy correlations. These governing correlations were solved using the Finite Volume Method, a numerical approach. The RANS equations are derived by disintegrating the flow variables into time-averaged and fluctuating components. This involves replacing the decomposed variables into the continuity, momentum, and energy correlations and then time-averaging the results. The RANS relationships can be mathematically expressed as follows [29,30].

Continuity Equation: This equation demonstrates how mass is maintained constant in a control volume. It states that, in the absence of net creation or loss of mass, the rates of entry and exit of mass into and out of a system are equal.

$$\frac{\partial \rho}{\partial t} + \frac{\partial \rho u}{\partial x} + \frac{\partial \rho v}{\partial y} + \frac{\partial \rho w}{\partial z} = 0 \qquad (1)$$

Momentum Equation: This equation, which comes from Newton's second law, explains how momentum is conserved. The left-hand side shows the transient and convective acceleration, and the right-hand side shows the pressure forces, viscous forces, and body forces (like gravity). It controls how the system's velocity fields change [30,31].

$$\frac{\partial \rho u}{\partial t} + \nabla.(\rho u V) = -\frac{\partial p}{\partial x} + \mu\left(\frac{\partial^2 u}{\partial x^2} + \frac{\partial^2 u}{\partial y^2} + \frac{\partial^2 u}{\partial z^2}\right) + \rho f x \quad (2)$$

$$\frac{\partial \rho v}{\partial t} + \nabla.(\rho v V) = -\frac{\partial p}{\partial y} + \mu\left(\frac{\partial^2 v}{\partial x^2} + \frac{\partial^2 v}{\partial y^2} + \frac{\partial^2 v}{\partial z^2}\right) + \rho f y \quad (3)$$

$$\frac{\partial \rho w}{\partial t} + \nabla.(\rho w V) = -\frac{\partial p}{\partial z} + \mu\left(\frac{\partial^2 w}{\partial x^2} + \frac{\partial^2 w}{\partial y^2} + \frac{\partial^2 w}{\partial z^2}\right) + \rho f z \quad (4)$$

V and u, v, w, are the flow vector velocity and velocity components in (x, y, z) space. t is the operational time, and f is the body force per unit mass. μ is absolute viscosity, and ρ is air density.

Energy Equation: This equation prevents energy loss. Energy storage and unstedy distribution are shown on the right side, while conduction is shown on the left side. Understanding the distribution of heat across the working fluid and the boundaries of the system depends on it [30,31].

$$\frac{\partial^2 T}{\partial x^2} + \frac{\partial^2 T}{\partial y^2} + \frac{\partial^2 T}{\partial z^2} = \frac{\rho C p}{k}\frac{\partial T}{\partial t} \quad (5)$$

For the SAH absorber plate and airflow [29-31]:

$$\frac{\partial(\rho C p T)}{\partial t} + \nabla.(\rho C p V T) = \nabla.(k \nabla T) + gV + \rho T \frac{DCp}{Dt} \quad (6)$$

k is the thermal conductivity, and g signifies the rate of heat source within the material per unit volume.

The turbulence kinetic energy (k) and its dissipation rate (ε). Eq. 7 can determine the turbulence kinetic energy (k) [29-31],

$$\frac{\partial}{\partial t}(\rho k) + \frac{\partial}{\partial x_i}(\rho k u_i) = \frac{\partial}{\partial x_j}\left[\left(\mu + \frac{\mu_t}{\sigma_k}\right)\frac{\partial k}{\partial x_j}\right] + G_k + G_b - \rho\epsilon - Y_M + S_k \quad (7)$$

Eq. 8 signifies the rate of dissipation (ε) [29-31],

$$\frac{\partial}{\partial t}(\rho \varepsilon) + \frac{\partial}{\partial x_i}(\rho \varepsilon u_i) = \frac{\partial}{\partial x_j}\left[\left(\mu + \frac{\mu_t}{\sigma_\varepsilon}\right)\frac{\partial \varepsilon}{\partial x_j}\right] + C_{1\varepsilon}\frac{\varepsilon}{k}(G_k + C_{3\varepsilon}G_b) - C_{2\varepsilon}\rho\frac{\varepsilon^2}{k} + S_\varepsilon \quad (8)$$

Referring to S_k and S_ε, it can be quantified as a constant or user-defined source term, but it is considered zero by default. Eq. 9 can be used to find the turbulent viscosity. μ_t [29-31],

$$\mu_t = \rho C_\mu \frac{k^2}{\varepsilon} \quad (9)$$

The mean velocity gradients G_k can be estimated using Eq. 10, which can signify the generation of turbulence kinetic energy [29-31],

$$G_k = -\rho \underline{\acute{u}_i \acute{u}_j} \frac{\partial u_j}{\partial x_i} \quad (10)$$

The Reynolds stresses $(-\rho \underline{\acute{u}_i \acute{u}_j})$ is stated as follows [29-31],

$$-\rho \underline{\acute{u}_i \acute{u}_j} = \mu_t\left(\frac{\partial u_i}{\partial x_j} + \frac{\partial u_j}{\partial x_i}\right) - \frac{2}{3}\left(\rho k + \mu_t \frac{\partial u_k}{\partial x_k}\right)\delta_{ij} \quad (11)$$

$\acute{u}_i$ and $\acute{u}_j$ are the fluctuating velocity components (i=1, 2, 3). The buoyancy G_b can be expressed in the following equation, which can be used to generate the turbulence kinetic energy [29-31],

$$G_b = \beta g_i \frac{\mu_t}{Pr_t}\frac{\partial T}{\partial x_i} \quad (12)$$

g_i Is the component of the gravitational vector.

Pr_t is the turbulent Prandtl number for energy ($Pr_t = 0.85$), and β is the coefficient of thermal expansion.

The fluctuated dilatation in compressible turbulence to the overall dissipation rate is represented in Eq. 13 [29-31],

$$Y_M = 2\rho\varepsilon M_t^2 \quad (13)$$

σ_k and σ_ε are the turbulent Prandtl numbers for k and ε, and the model constants have the following default values [32]: $C_{1\varepsilon}$ = 1.44, $C_{2\varepsilon}$ = 1.92, $C_{3\varepsilon}$ = 1, $\sigma_k = 1$, σ_ε = 1.3, = 0.09

2.6 Performance parameter

The assessment of the collector's performance is carried out by analysing the key parameters, namely the average Nusselt number (Nu), the coefficient of friction (f), and the thermal-hydraulic performance parameter (THPP) across a range of Re as elucidated below.

$$Re = \frac{\rho\, u\, Dh}{\mu} \quad (14)$$

$$Nu = \frac{h\, Dh}{k} \quad (15)$$

The hydraulic diameter (Dh) for the rectangular channel of the SAH can be calculated as follows [32].

$$Dh = \frac{4\,Ac}{p} \quad (16)$$

The convection heat transfer coefficient can be evaluated based on experimental data using the following equations [33].

$$h = \frac{Q_{in}}{As(Ts - TiN)} \quad (17)$$

Q_{in} Is the heat transferred from the DPSAH absorber plate to the air as depicted in Eq. 19 [34],

$$Q_{in} = m\ c_p\ (T_O - T_{in}) \quad (18)$$

The high-pressure loss produced in an enlarged fan is due to energy use. Therefore, this research presented the notion of efficiency of cf = 0.18 to balance both collection efficacy and pressure loss [35,36].

$$\eta_{eco} = \frac{Q_{in} - \frac{A\ U\ \Delta p}{cf}}{A_s\ \alpha\ \beta\ I} \quad (19)$$

The non-dimensional friction coefficient (*f*) can be calculated using Eq. 21 while considering the average velocity (U), and pressure drop per unit length (Δp/l), as follows [17].

$$f = \frac{2\ \Delta p\ D_h}{4\ l\ \rho\ U^2} \quad (20)$$

$$\text{THPP} = \frac{\frac{nu}{nu_s}}{\left(\frac{f}{f_s}\right)^{\frac{1}{3}}} \quad (21)$$

In the base mode, where no turbulator is presented inside the SAH, (Nu) and the friction factor can be assessed. Another significant consideration is the pumping power, which openly affects the economic viability of the system, which can be assessed utilising the following relationships [17].

$$Nu_s = 0.023\ Re^{0.8} Pr^{0.4} \quad (22)$$

$$f_s = 0.085\ Re^{-0.25} \quad (23)$$

$$p_m = \frac{m\ \Delta p}{\rho} \quad (24)$$

2.7 Mesh Generation

The mesh tool in COMSOL Multiphysics 6.1V was utilised to form the structural mesh of SAH by dividing the computational domain into a large number of individual elements that differ in shape and size to solve mathematical equations and analyse the flow field, as shown in Fig. 4. The data of the mesh independence test for the outlet temperatures are depicted in Fig. 5. Fig. 5 shows changes in outlet temperature with the number of elements. Therefore, simulations are the best outlet for 1.05 million elements. The flow turbulators and absorber plates are shown to have small element sizes for the accuracy of the solution.

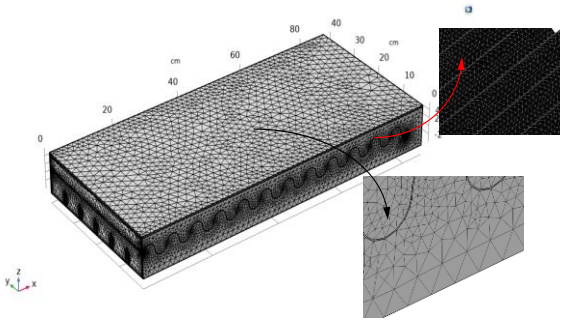

Figure 4. Meshing generation

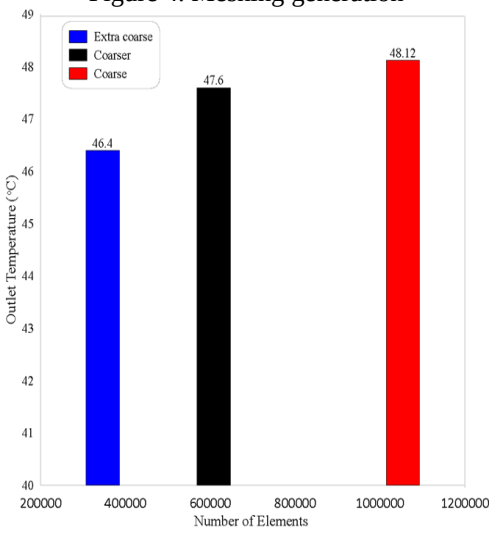

Figure 5. Changes in outlet temperature against the number of elements

3. Results and Discussion

To authenticate the accuracy of the current numerical models, the temperature contours of the absorber plates from the numerical findings of Chang et al. 2024 [19] were compared against the currently predicted outcomes, as illustrated in Figure 6. The temperatures of the simulated absorber plates matched well with the results of Chang et al. (2024) [19]. The most significant and average relative variances of the temperatures are 128 °C and 130 °C, respectively. The experimental results of the SAH provided by Abd et al. (2022) [37] were also compared against the current results, as shown in Figure 7. The simulated efficiency closely aligned with the experimental results. The extreme and average relative efficiency deviances are 66% and 70%, respectively. The discrepancies between the calculated efficiency and the experimental results can be attributed to the constant ambient wind velocity assumption in the current simulation.

Figure 8 illustrates the patterns of solar radiation and ambient temperature for January 12, 2025. Solar radiation increases from 9 AM to 2 PM and diminishes thereafter. The results indicate that this day's maximum solar radiation value was 750 W/m² (at 2 PM). The maximum variation in ambient temperature did not exceed 10 °C. Furthermore, the results indicate that the maximum ambient temperature for this day was recorded at 35 °C (at 1 PM).

Figure 9 illustrates the airflow velocity streamlines within the double-pass solar collector. It also demonstrates that using a roughness plate in the channel can correlate with an increased turbulent flow regime. Specifically, this results from the mixing effect produced by the air and fins. The turbulent flow can impact the heat transfer rate, resulting in an elevated exit temperature. Due to the absence of fins, it achieves a standard air distribution after traversing the lower section.

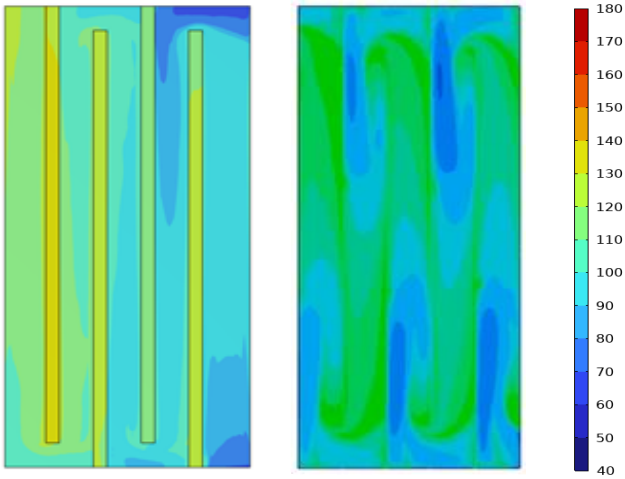

Current research (Chang et al., 2024) [19]

Figure 6. Temperature contours of the absorber plates validation

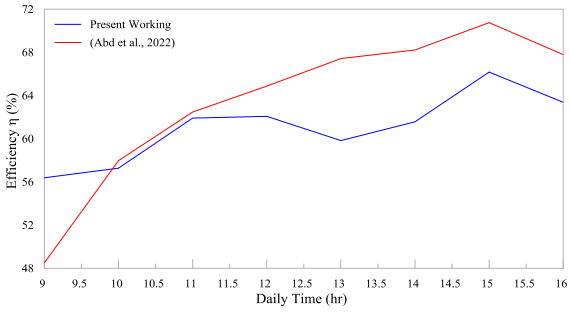

Figure 7. Efficiency comparison against the experimental results of [37]

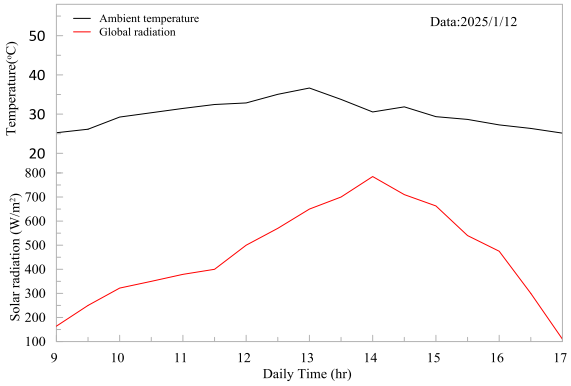

Figure 8. Deviation of the solar radiation and ambient temperature

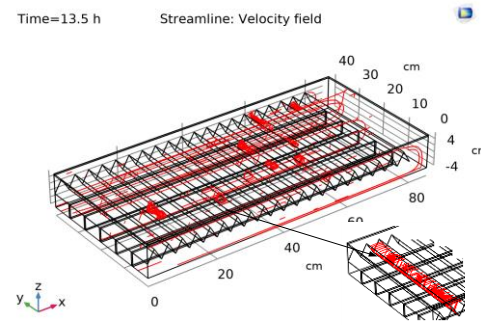

(a)

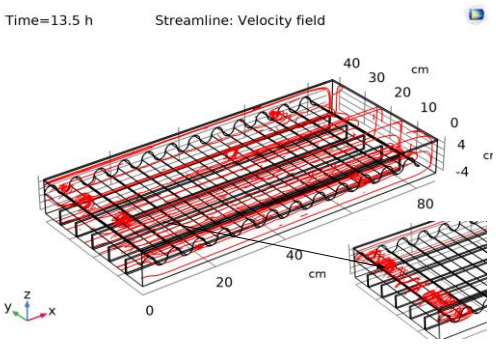

(b)

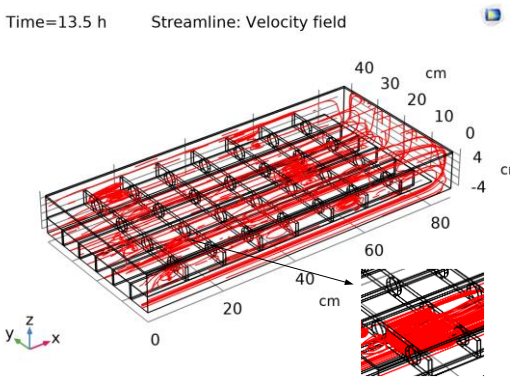

(c)

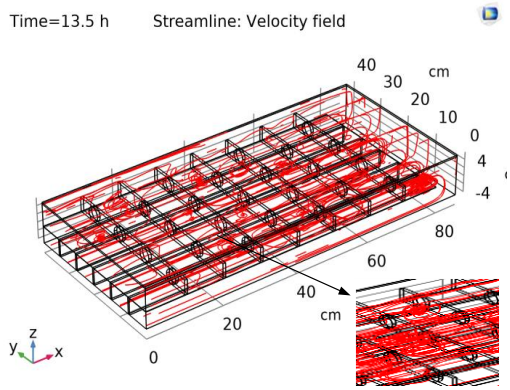

(d)

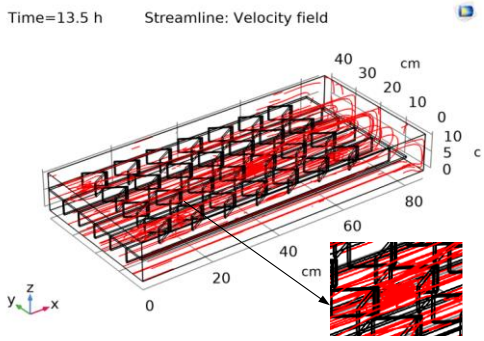

(e)

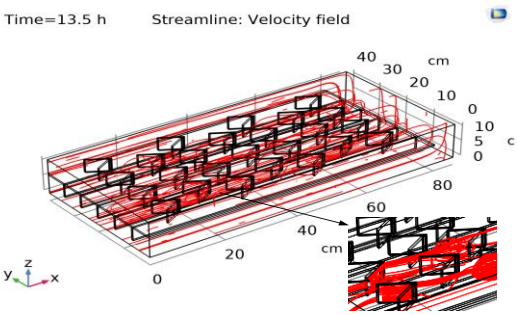

(f)

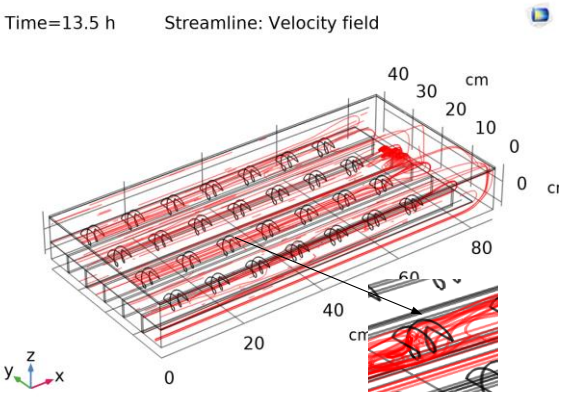

(G)

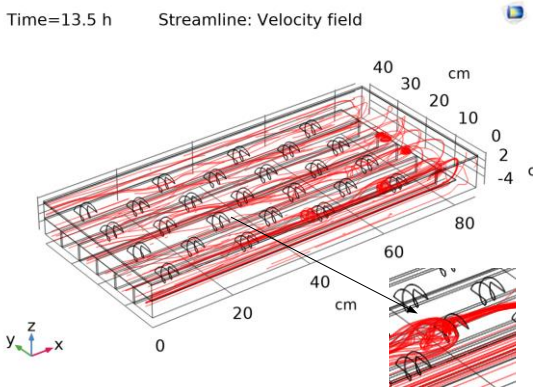

(H)

Figure 9. Velocity streamlines within the double-pass solar collector. (A) corrugate plate, (B) wave plate, (C) orifice fins in line, (D) orifice fins staggered, (E) V-ribs in line, (F) V-ribs staggered, (G) S-ribs in line, (H) S-ribs staggered

To further elucidate the effect of the revised arrangement of the absorber plate on system performance, the fluctuations in plate temperature (TP) and outlet temperature (Tout) have been depicted in Figure 10. Figure 10 demonstrates that Tout and TP commence their rise after 9 AM, reaching the maximum value at 2:00 PM and dropping after 3 PM. The optimal values of Tout have consistently been identified when employing wave plate configurations. In contrast, the peak values of TP have been noted across all configurations compared to the smooth variant. This indicates that the wave plate structure is more effective than alternative methods for heat transfer processes. Figure 11 illustrates the variation of effective efficiency across all roughness geometries. The effective efficiency of the rough duct across all roughness geometries exceeds that of the smooth duct. In all instances, the effective efficiency remains elevated across all roughness geometries, as a rise in the Re augments flow turbulence, reduces the thickness of the thermal boundary layer, and recovers the convective heat transfer rate. An analysis of the presentation of various roughness setups is depicted in Figure 11, which reveals that orifice fins and inline elements exhibit the lowest effective efficiency, whilst the wave plate demonstrates the highest effective efficiency.

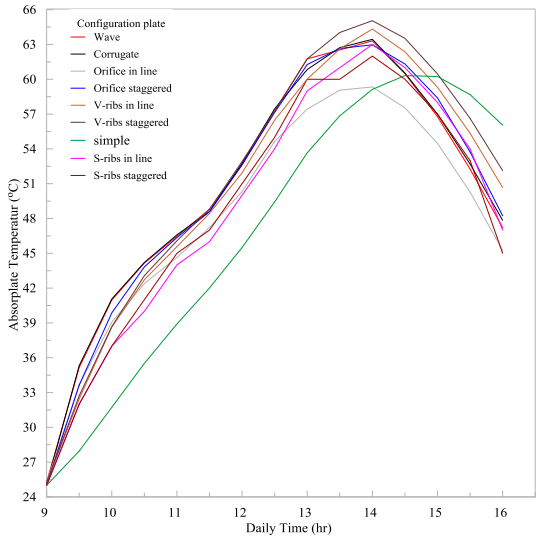

(a)

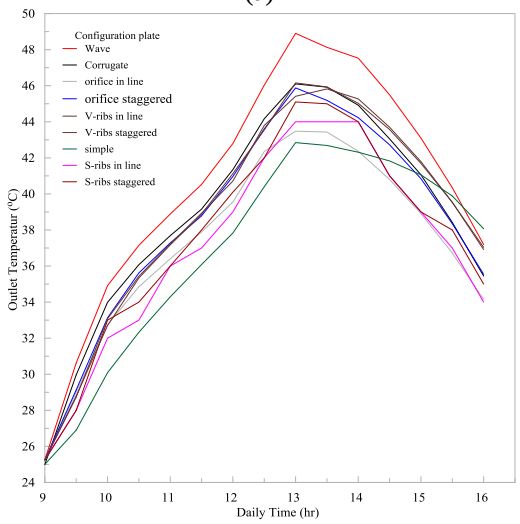

(b)

Figure 10. Variation of the temperature in SAH, (a) plate temperature, (b) outlet temperature

Figure 11 illustrates the variation of effective efficiency across all roughness geometries. The effective efficiency of the rough duct across all roughness geometries exceeds that of the smooth duct. In all instances, the effective efficiency remains elevated across all roughness geometries, as a rise in the Re augments flow turbulence, reduces the thickness of the thermal boundary layer, and recovers the convective heat transfer rate. An analysis of the presentation of various roughness setups is depicted in Figure 11, which reveals that orifice fins and inline elements exhibit the lowest effective efficiency, whilst the wave plate demonstrates the highest effective efficiency.

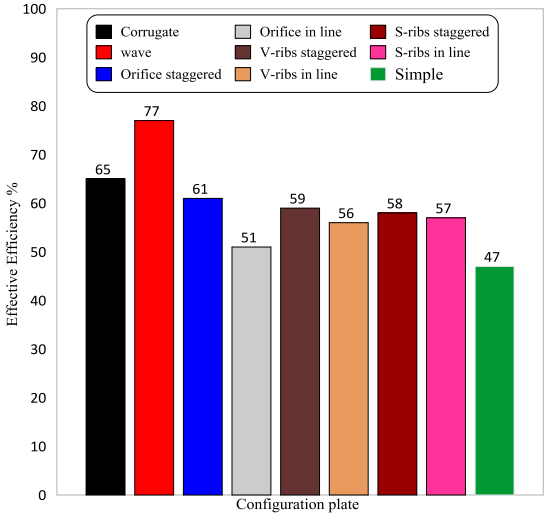

Figure 11. Variation of effective efficiency across all roughness geometries

Thus, Figures 10 and 11 can provide conclusive evidence that the wave plate outperforms the other configuration for effective efficiency and outlet temperature. Thus, the current research focuses on the performance of the SAH when wave plates are used as absorber plates.

Figure 12 illustrates the pressure drop and output temperature over time at various mass flow rates for the SAH with a wave plate as an absorber plate. The pressure decrease is a notable concern pertinent to this topic, which must be incorporated into the ongoing inquiry. The results indicate that the pressure drop has increased with an air mass flow rate elevation.

At a solar irradiation of 650 W/m², the maximum recorded outlet temperatures are 50 °C, 45 °C, and 40 °C for mass flowrates of 0.01 kg/s, 0.015 kg/s, and 0.02 kg/s, respectively. This implies that a rise in mass flow rate can cause a reduction in the outlet temperature. Accordingly, it can be said that a rise in the air flow rate can minimise the total heat loss.

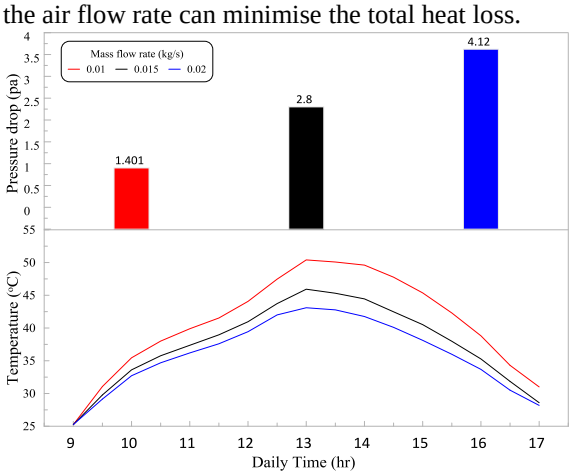

Figure 12. Pressure drop and output temperature against time at various mass flow rates for the SAH with a wave plate as an absorber plate

Figure 13 illustrates the power consumed to generate the required mass flow rate, which is naturally increased as a result of the rise in the flow rate and associated high pressure drop, with an increase near the expansion. Thus, it can be said that a high flow rate can ascertain a higher generated power.

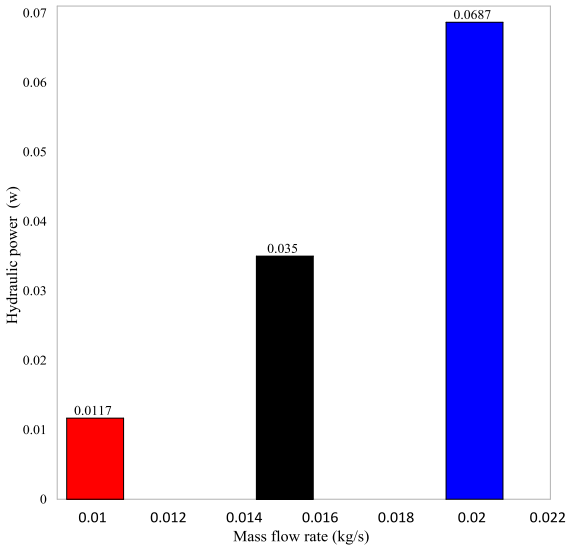

Figure 13. Mass flow rate and hydraulic power

Figure 14 illustrates the fluctuation of the average Nu about the Re for two scenarios: one with a wave plate and the other with a smooth plate. The average Nusselt number is detected to grow with a rise in the Re, which is consistent with the existing understanding. As the Re increases, the thickness of the laminar sub-layer diminishes, leading to improved heat transmission due to the eddies and circulations generated by the wave plate. The improvement in heat transfer rate surpasses that of the smooth surface. The wave plate's precise configuration can significantly influence the magnitude of this enhancement.

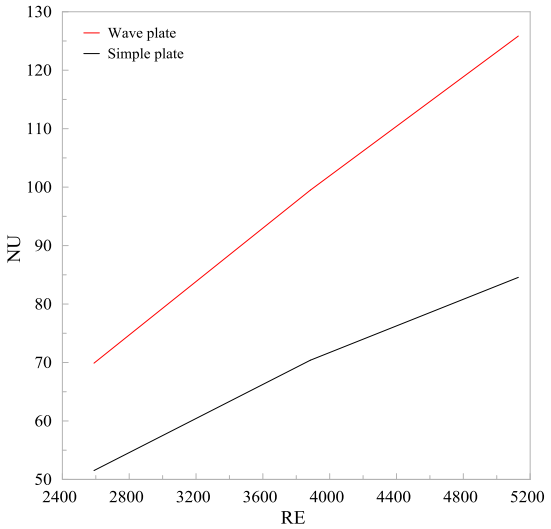

Figure 14. Nusselt number as a function of the Reynolds number

Figure 15 illustrates the correlation between the average f in two scenarios: one with a wave plate and the other with a smooth plate. The average f diminishes as the Re rises. The average friction coefficient with the wave plate is greater than that without it or in a smooth duct across the whole range of Re.

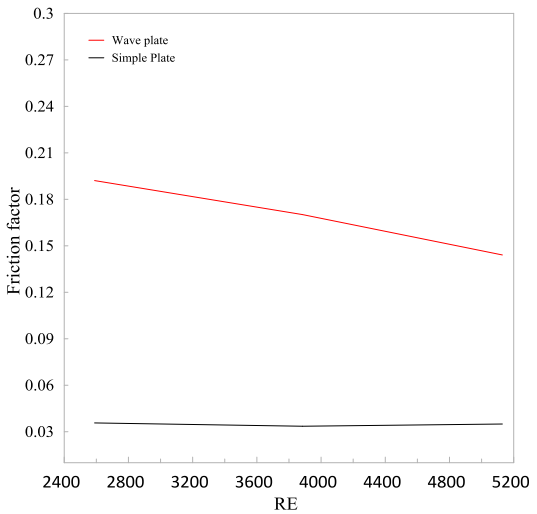

Figure 15. Friction factor as a function of the Reynolds number

Figure 16 illustrates the relationship between thermos-hydraulic performance (THPP) and Reynolds number in the wave plate SAH. It indicates that as the Reynolds number grows, the value of THPP also rises. The acquired values for THPP exceed 1, indicating that the increase in heat transfer from the plate to the air surpasses frictional losses or pumping power.

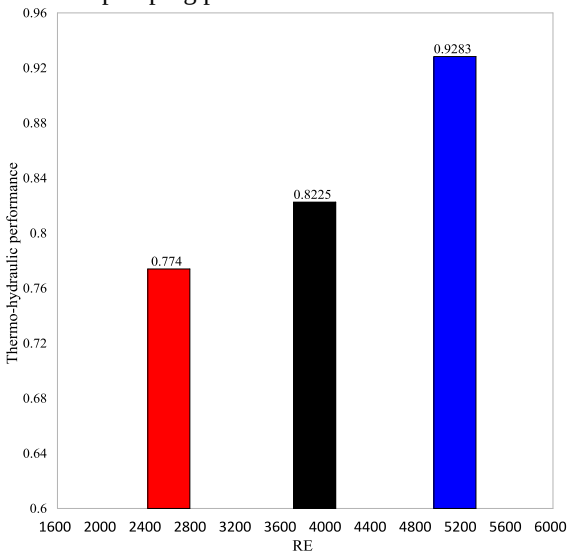

Figure 16. THPP as a function of the Reynolds number

4. Conclusions

The current research examined the thermal and frictional properties of an SAH fitted with turbulators of diverse forms and setups. The emphasis was on contrasting the performance of the SAH equipped with turbulators against a smooth SAH devoid of them. The principal conclusions of the study can be encapsulated as follows.

1- A turbulator in the absorber portion markedly improved the thermal performance relative to a smooth SAH.

2- The utilisation of a roughness plate in the channel correlated with an increase in the turbulent flow regime.

3- The pressure drop increased, while the outlet temperature decreased as the air flow rate increased.

4- The wave plate had a significantly higher exit temperature and effective efficiency compared to the other cross-sectional geometries.

5- The average Nu improved while the friction factor decreased as the air flow rate's velocity increased.

6-The amount of energy needed to produce the necessary mass flow rate, which is inevitably raised due to the increase in flow rate and the corresponding high-pressure drop.

7-The average friction coefficient with the wave plate is higher than without it or in a smooth duct.

8-The value of thermos-hydraulic performance THPP increases with the Reynolds number.

9-The enhanced heat transfer rate of a wave plate is substantially higher than that of a smooth surface.

5. Future Scope

This study highlights the significance of baffle positioning in enhancing the thermo-hydraulic efficiency of DPSAHs. This work suggests several potential avenues for future research.

1. Experimental validation: Fabricating and evaluating prototypes to ascertain the accuracy of numerical data in practical scenarios.

2. Advanced optimisation: Employing artificial intelligence and multi-objective optimisation techniques to determine the optimal configuration of baffle placement and design.

3. Hybrid integration: Incorporating the proposed design into PV/T systems or solar-assisted heat pump configurations to optimise their efficiency.

Nomenclature

Symbol	Definition
CFD	Computational Fluid Dynamics
Cp	Specific heat at constant pressure (J/kg·K)
Dh	Hydraulic diameter (m)
DPSAH	Double-Pass Solar Air Heater
d1, d2	Characteristic diameters in frustum elements (m)
f	Friction factor (–)
FP_SAH	Flat Plate Solar Air Heater
Gk	Generation of turbulence kinetic energy (m^2/s^3)
h	Convective heat transfer coefficient ($W/m^2·K$)
H	Channel height (m)
k	Thermal conductivity (W/m·K)
k	Turbulence kinetic energy (m^2/s^2)
L	Channel length (m)
μ	Dynamic viscosity (Pa·s)
Nu	Nusselt number (–)
PCM	Phase Change Material
q	Heat flux (W/m^2)
RANS	Reynolds-Averaged Navier–Stokes
Re	Reynolds number (–)
ρ	Air density (kg/m^3)

SAH	Solar Air Heater
σk, σε	Turbulent Prandtl numbers for k and ε
Ta	Ambient temperature (°C)
THPP	Thermo-hydraulic performance parameter (–)
t/L	Thickness-to-length ratio of PCM container (–)
Tp	Plate temperature (°C)
Tout	Outlet air temperature (°C)
TR_SAH	Transverse Solar Air Heater
u, v, w	Velocity components in x, y, z directions (m/s)
U	Average flow velocity (m/s)
W	Channel width (m)
YM	Contribution of fluctuating dilatation (–)
Δp	Pressure drop (Pa)
ε	Turbulence dissipation rate (m^2/s^3)
ηth	Thermal efficiency (%)
νt	Turbulent viscosity (m^2/s)

References

1. Rashid, F. L., Al-Obaidi, M. A., Hussein, A. K., Akkurt, N., Ali, B., and Younis, O. (2022). Floating solar stills and floating solar-driven membranes: Recent advances and overview of designs, performance and modern combinations. *Solar Energy*, *247*, 355–372. https://doi.org/10.1016/j.solener.2022.01.042
2. Khullar, V., Mahendra, P., and Mittal, M. (2018). Applicability of heat mirrors in reducing thermal losses in concentrating solar collectors. *Journal of Thermal Science and Engineering Applications*, *10*(6), 061004. https://doi.org/10.1115/1.4040576
3. Boudhiaf, R., Touhami, Y., Harby, K., Kabeel, A. E., Attia, M. E. H., Khelifa, A., Latrache, N., and Driss, Z. (2025). Enhancing the thermal performance of solar air heaters using heat storage medium: An experimental study with energy, exergy, and economic approach. *Journal of Thermal Science and Engineering Applications*, *17*(6). https://doi.org/10.1115/1.4065533
4. Kumar, D., Layek, A., Kumar, A., and Kumar, R. (2024). Experimental study for the enhancement of thermal efficiency and development of Nusselt number correlation for the roughened collector of solar air heater. *Journal of Thermal Science and Engineering Applications*, *16*(2). https://doi.org/10.1115/1.4057918
5. Kareem, F. A., Skheal, O. R., and Lafta, N. S. (2022). Experimental study and exergy analysis about the flat plate solar collector. *International Journal of Integrated Engineering*, *14*(6), 156–171. https://doi.org/10.30880/ijie.2022.14.06.014
6. Bensaci, C. E., Moummi, A., Sanchez de la Flor, F. J., Rodriguez Jara, E. A., Rincon-Casado, A., and Ruiz-Pardo, A. (2020). Numerical and experimental study of the heat transfer and hydraulic performance of solar air heaters with different baffle positions. *Renewable Energy*, *155*, 1231–1244. https://doi.org/10.1016/j.renene.2020.04.017
7. Khalifa, A. H. N., and Kareem, F. A. (2022). Development of exergy maps as a tool for assessing solar energy potential in Iraq. *International Journal of Exergy*, *37*(2), 145–158. https://doi.org/10.1504/IJEX.2022.122170
8. Kareem, F. A., Khalifa, A. H. N., and Hamad, A. J. (2024). Numerical analysis of two-bed adsorption thermophysical battery. *Applied Thermal Engineering*, *236*, 121847. https://doi.org/10.1016/j.applthermaleng.2023.121847
9. Ghanem, S. R., and Bhosale, A. C. (2024). Honeycomb-shaped artificial roughness in solar air heaters: CFD-experimental insights into thermo-hydraulic performance. *Renewable Energy*, *230*, 120829. https://doi.org/10.1016/j.renene.2024.120829
10. Kareem, F. A., Alsayah, A. M., Alshukri, M. J., Ali, S., Faraj, J., and Khaled, M. (2025). Advancing sustainable refrigeration: Ejector expansion refrigeration cycles for energy efficiency and environmental protection. *Results in Engineering*, *26*, 104926. https://doi.org/10.1016/j.rineng.2025.104926
11. Kareem, F. A., Hamad, A. J., and Khalifa, A. H. N. (2024). Experimental investigation of two-bed adsorption thermophysical battery with mass recovery technology. *Energy Conversion and Management*, *309*, 118460. https://doi.org/10.1016/j.enconman.2024.118460
12. A. Abdul Kareem, H., Khalifa, A., and Hamad, A. (2024). Investigation of Photovoltaic Membrane Desalination Utilizing Storage Heat in Solar Cells. International Journal of Thermodynamics, 27(3), 6-14. https://doi.org/10.5541/ijot.1390518
13. Debnath, S., Das, B., Randive, P. R., and Pandey, K. M. (2018). Performance analysis of solar air collector in the climatic condition of

North Eastern India. *Energy*, *165*, 281–298. https://doi.org/10.1016/j.energy.2018.09.038

14. Singh, S., Chaurasiya, S. K., Negi, B. S., Chander, S., Nemś, M., and Negi, S. (2020). Utilizing circular jet impingement to enhance thermal performance of solar air heater. *Renewable Energy*, *154*, 1327–1345. https://doi.org/10.1016/j.renene.2020.03.095
15. Hassan, H., and AboElfadl, S. (2021). Heat transfer and performance analysis of SAH having new transverse finned absorber of lateral gaps and central holes. *Solar Energy*, *227*, 236–258. https://doi.org/10.1016/j.solener.2021.08.061
16. Iqbal, M. H., et al. (2023). Numerical analysis of a novel solar air heater design with V-ribs and jet cooling. *Sustainable Energy Technologies and Assessments*, *57*, 103252. https://doi.org/10.1016/j.seta.2023.103252
17. Hamad, R. F., Alshukri, M. J., Eidan, A. A., and Alsabery, A. I. (2023). Numerical investigation of heat transfer augmentation of solar air heater with attached and detached trapezoidal ribs. *Energy Reports*, *10*, 123–134. https://doi.org/10.1016/j.egyr.2023.06.031
18. Singh, D., and Kumar, V. (2024). Response surface-based optimization of thermal characteristics for frustum roughened solar air heater: An experimental and numerical study. *International Journal of Heat and Fluid Flow*, *108*, 109479. https://doi.org/10.1016/j.ijheatfluidflow.2024.109479
19. Chang, Y., Xue, Y., and Geng, G. (2024). Effect of the baffle's type on thermal performance of solar air heaters. *Case Studies in Thermal Engineering*, *59*, 104580. https://doi.org/10.1016/j.csite.2024.104580
20. Yusaidi, N. J., Fauzan, M. F., Abdullah, A. F., Ibrahim, A., and Ishak, A. A. (2024). Theoretical and experimental investigations on the effect of double pass solar air heater with staggered-diamond shaped fins arrangement. *Case Studies in Thermal Engineering*, *60*, 104619. https://doi.org/10.1016/j.csite.2024.104619
21. Salarpour, N., and Azadani, L. N. (2024). Optimization and evaluation of thermo-hydraulic performance of solar air heaters equipped with different roughness geometries. *Case Studies in Thermal Engineering*, *61*, 105037. https://doi.org/10.1016/j.csite.2024.105037
22. Rawat, P., Ashwni, and Sherwani, A. F. (2024). Optimization of single and double pass solar air heater-phase change material (SAH-PCM) system based on thickness to length ratio. *International Journal of Heat and Mass Transfer*, *224*, 125356. https://doi.org/10.1016/j.ijheatmasstransfer.2024.125356
23. Dong, S., Di, Y., Gao, Y., Long, H., Fan, Z., Guan, J., Han, L., and Wang, Y. (2025). Multiple operational strategies investigations of the PV/T collectors based on 3 days ahead hourly radiation prediction. *Applied Energy*, *377*, 124383. https://doi.org/10.1016/j.apenergy.2024.124383
24. Rashid, F. L., Rahbari, A., Ibrahem, R. K., Talebizadehsardari, P., Basem, A., Kaood, A., Mohammed, H. I., Abbas, M. H., and Al-Obaidi, M. A. (2023). Review of solidification and melting performance of phase change materials in the presence of magnetic field, rotation, tilt angle, and vibration. *Journal of Energy Storage*, *67*, 107501. https://doi.org/10.1016/j.est.2023.107501
25. Hussein, A. K., Togun, H., Rashid, F. L., Basem, A., Abed, A. M., Al-Obaidi, M. A., Abdulrazzaq, T., Dhabab, J. M., Attia, M. E. H., Ali, B., and Rout, S. K. (2025). Mixed convection in trapezoidal enclosures containing mono and hybrid nanofluids: A comprehensive review. *Journal of the Brazilian Society of Mechanical Sciences and Engineering*, *47*(4), 176. https://doi.org/10.1007/s40430-024-05013-9
26. Rashid, F. L., Al-Gaheeshi, A. M. R., Al-Obaidi, M. A., Mohammed, H. I., Togun, H., and Agyekum, E. B. (2024). Analysing fluid flow and heat transfer comparatively in flow passage systems: Evaluating thermal impacts and geometric configurations. *International Journal of Thermofluids*, *24*, 100894. https://doi.org/10.1016/j.ijft.2024.100894
27. Rashid, F. L., Hussein, A. K., Al-Obaidi, M. A., Alshammari, B. M., Ali, B., Hajlaoui, R., Boudabous, M. M., and Kolsi, L. (2024). A review of radiant heating and cooling systems incorporating phase change materials. *Journal of Thermal Analysis and Calorimetry*, *149*(15), 7891–7917. https://doi.org/10.1007/s10973-024-13065-0
28. Rashid, F. L., Al-Obaidi, M. A., Mahdi, A. J., and Ameen, A. (2024). Advancements in Fresnel lens technology across diverse solar energy applications: A comprehensive review.

Energies, *17*(3), 569. https://doi.org/10.3390/en17030569

29. Hashemian, N., and Noorpoor, A. (2023). Thermo-eco-environmental Investigation of a Newly Developed Solar/wind Powered Multi-Generation Plant with Hydrogen and Ammonia Production Options. Journal of Solar Energy Research, 8(4), 1728-1737. https://doi:10.22059/jser.2024.374028.1388
30. Smith, J. M. (1950). Introduction to chemical engineering thermodynamics. Journal of *Chemical Education*, *27*(10), 584. https://doi.org/10.1021/ed027p584.3 ACS Publications
31. Bergman, T. L., Lavine, A. S., Incropera, F. P., and DeWitt, D. P. (2011). *Fundamentals of heat and mass transfer* (7th ed.). John Wiley and Sons.
32. Naji, A. A., Daud, H. A., Yasin, N. J., and Jasim, A. A. (2023). Experimental Study of Two Rows Hybrid Film Cooling Holes Over Flat Plate Surface Using IR Technology. Journal of Techniques, 5(3), 108-115. https://doi.org/10.51173/jt.v5i3.1231
33. Aktas, M. F., Sözen, A., Tuncer, A. D., Arslan, E., Koşan, M., and Çürük, O. (2019). Energy-exergy analysis of a novel multi-pass solar air collector with perforated fins. *International Journal of Renewable Energy Development*, *8*(2), 151–160. https://doi.org/10.14710/ijred.8.2.151-160
34. Chinnappan, T., C.M, R., Dhairiyasamy, R., and Rajendran, S. (2024). Comparative Analysis of Polycarbonate and Glass Cover Configurations for Enhanced Thermal Efficiency in Flat Plate Solar Collectors for Water Heating. Journal of Solar Energy Research, 9(1), 1794-1810. https://doi: 10.22059/jser.2024.374268.1394
35. Hamad, A. J., Hussien, F. M., and Faraj, J. J. (2021). Multiple phase change materials for performance enhancement of a solar dryer with double pass collector. *Energy Engineering: Journal of the Association of Energy Engineering*, *118*(5), 1483–1497. https://doi.org/10.32604/ee.2021.016867
36. Kareem, F. A., Khalifa, A. H. N., and Hamad, A. J. (2024). Intermittent and continuous adsorption refrigeration systems techniques: A review. *AIP Conference Proceedings*. https://doi.org/10.1063/5.0212206
37. Abd, H. M., Alomar, O. R., and Salih, M. M. M. (2022). Improving the performance of solar air heater using a new model of V-corrugated absorber plate having perforations jets. *International Journal of Energy Research*, *46*(6), 8130–8144. https://doi.org/10.1002/er.7715

Appendix A

Table A1. A summary of relevant studies of solar air heaters

Authos (Year)	Study type	Configuration / Feature	Operating range / Setup	Key reported metrics	Relevance to current simulation
Debnath et al. (2018) [13]	Experimental	Solar air collector (single vs. double glazing; corrugated plates)	Air ṁ varied; North-East India climate	Double glazing > single; corrugation ↑ efficiency by ~14%; peak exergy gain ~6.867% at ṁ=0.0118 kg/s	Supports higher ṁ and surface texturing in model validation
Singh et al. (2020) [14]	Experimental	Impinging jet double-pass SAH (with/without porous media)	Comparative tests	Max thermal eff. 94% (no porous); THPP 84%; ~7.5–19% higher than porous	Corroborates jet-enhanced convection assumptions and the THPP method
Hassan and AboElfadl (2021) [15]	Experimental	Transverse SAH, single vs double pass	High ṁ up to 0.075 kg/s	Energy eff. ≈ 89% (double), ~24% higher than flat; low pumping penalty	Supports double-pass design and inclusion of fan power term
Iqbal et al. (2023) [16]	Numerical (CFD)	Impinging jets + rectangular V-ribs	Baseline SAH comparison	Nu ×3.36; f ×5.31 vs traditional SAH	Validates rib/jet interaction and Nu–f trade-off trends
Hamad et al. (2023) [17]	Numerical (RNG k-ε)	Trapezoidal ribs (attached/detached)	Parametric Re sweep	Best thermal when ribs are against the flow; performance ↓ with rib height growth	Back rib orientation and geometry sweep
Singh and Kumar (2024) [18]	Exp. + Simulation	Frustum-shaped roughness; optimize e/Dh, e/d1, d1/d2	Re ≈ 12,500	Optimal Nu ≈ 256.8; min f≈0.009; desirability=0.0905	Provides validated parametric bounds for optimisation
Chang et al. (2024) [19]	Numerical	Transverse baffles; varying count	ṁ=0.026–0.078 kg/s	η peaks at N=4 for 0.026 (≈54.3%); N=6 best at higher ṁ (60–64%)	Supports discrete baffle-count as a design variable
Yusaidi et al. (2024) [20]	Theoretical + Exp.	DPSAH with staggered diamond fins	ṁ up to 0.0261 kg/s; G=1000 W/m²	Max η:exp=59.3%, sim=62.0%; η rises with flow rate.	Confirms exp–sim agreement tolerance and $\partial\eta/\partial\dot{m}$
Salarpour and Azadani (2024) [21]	Numerical	Six geometries (baffles, V-ribs, etc.)	Comparative study	Rectangular baffles have the highest Nu and THPP; inline cubes have the lowest.	Justifies geometry prioritization
Rawat and Sherwani (2024) [22]	Numerical (2D transient)	SAH with PCM	Single vs double pass; t/L optimisation	Optimal t/L ↑ liquid fraction to 0.976; ↓ dead length ~92%	Validates transient storage physics and PCM ratios
Dong et al. (2025) [23]	Exp./Techno-economic	Advanced PV/T with reflector, graphite, trapezoidal channels	Compared to fixed PV/T	Thermal +17.8%, electrical +13.6%; 39.5 MJ and 7.8 kWh per 2.08 m²	Corroborates channel-shape/hybrid strategies